

# Oscillatory shear flow in nanochannels via hybrid particle-continuum scheme

R. Delgado-Buscalioni\* and P. V. Coveney†  
Centre for Computational Science,  
Dept. Chemistry, University College London,  
Gower Street, London WC1 OAJ, U.K

E. G. Flekkøy‡  
Dept. of Physics, Oslo University,  
PB 1048 Blindern, 0316 Oslo, Norway  
(Dated: November 20, 2018)

This paper provides an application of our hybrid continuum-particle scheme to liquids by considering unsteady shear flows driven by wall oscillations in nano-slots. The particle region (P) adjacent to the wall, is described at the atomistic level by molecular dynamics, while the outer region (C), described by a continuum equation for the transversal momentum, is solved via a finite volume method. Both regions overlap in the “handshaking” region where a two-way coupling scheme (C→P and P→C) is implemented. A protocol for the C→P coupling was presented in a previous paper [Delgado-Buscalioni and Coveney, Phys. Rev. E, **67**, 046704 (2003)]; here we focus on the the P→C counterpart, that is, on the exchange of information from the microscopic to the continuum domain. We first show how to use the finite volume formalism to balance the momentum and mass fluxes across the P→C surface in such a way that the continuity of velocity is ensured. Then we analyse the effect of the fluctuations of the (P) stress tensor on the stability and accuracy of the numerical scheme. This analysis yields a condition which establishes a restriction on the resolution of the flow field that can be described by the hybrid method, in terms of the maximum frequency and wavenumber of the flow.

PACS numbers: 47.85.Np,47.11+j,02.70.Ns,68.08-p

## I. INTRODUCTION

Many systems, including complex flows near interfaces, wetting, drop formation, melting, crystal growth from a fluid phase, and moving interfaces of immiscible fluids or membranes, are governed by the dynamic interplay between the rapid atomistic processes occurring within a small localized region and the slow dynamics occurring within the bulk liquid. Such problems are too computationally expensive for any standard molecular dynamics simulation (MD). A promising alternative is to use hybrid particle/continuum algorithms which retain the atomistic description only where it is needed, and reduce the computational cost by solving the bulk flow by much faster continuum fluid dynamics methods.

Hybrid particle/continuum algorithms for solids [1] and gases [2] were the first to be fully developed in the literature. As also happens in theoretical descriptions, a hybrid description of the liquid state is the most challenging one. The general procedure is to connect the particle region (P), described by molecular dynamics, and the continuum region (C), described by continuum fluid dynamics (CFD), with a handshaking region comprised of two buffers: C→P and P→C. Most of the difficulties encountered when developing a hybrid scheme for liquids arise at the C→P buffer, where the molecular dynamics has to be reconstructed so as to adhere to the prescriptions coming from the C-flow. Within the P→C region the microscopic variables are coarse-grained to supply boundary conditions for the continuum domain, although within this domain the molecular dynamics are not directly altered and their motion is uniquely governed by the corresponding molecular interactions.

The kind of information to be transferred at the handshaking region has been the subject of some discussion. The first hybrid schemes to appear in the literature [see Delgado-Buscalioni and Coveney [3] and references therein] considered the coupling of momentum in steady shear flows using schemes based on *coupling-through-state*; in particular on matching the velocity of P and C within the overlapping region. Flekkøy *et al.* [4] introduced another coupling strategy based on the exchange of the fluxes of conserved quantities (from and to P and C) and they applied their scheme

---

\*r.delgado-buscalioni@ucl.ac.uk

†p.v.coveney@ucl.ac.uk

‡flekoy@fys.uio.no

to transversal momentum and mass transfer in steady (Poiseuille) flows. This work was subsequently generalized to include the energy exchange [5]. More recently, Delgado-Buscalioni and Coveney [3] introduced modifications into the flux-based C→P coupling to allow mass, momentum and energy transfers in time-dependent flows. In that work, the MD region is surrounded by a continuum description and the C→P protocol gives rise to the generalized boundary conditions for the particle system which provide the correct (hydrodynamic) propagation and relaxation of shear, sound and heat waves across the MD region [3]. The same study compares schemes based on coupling-through-fluxes and coupling-through-state in the simulation of a relaxing flow due to decaying pressure waves. The results showed that the imposition of the continuity of the thermodynamic variables alone does not provide the correct decay of the hydrodynamic modes and, for example, it yields a negative entropy production [3]. On the contrary, when using the flux-scheme the correct thermohydrodynamic behaviour was obtained.

We would like to stress that, although most of the applications that any hybrid method must address involve unsteady flows, the previously proposed hybrid schemes for liquids have barely even considered time-dependent scenarios. One of the main purposes of this paper is to study the applicability of the flux-scheme in the simulation of time-dependent shear flows, ranging from moderate to high characteristic frequencies. To that end we consider fluid flow in a slot driven by the oscillatory motion of one of the walls in its own plane (Stokes problem). This set-up retains the essential features encountered in unsteady shear flows while being analytically solvable. Oscillatory shear flow is widely used in rheological studies of complex fluids, such as polymer brushes (see Wijmans and Smit [6] for a recent review). These systems are good examples of typical applications of the hybrid scheme, which can treat the complex fluid region by MD and the momentum transfer from the bulk by continuum fluid dynamics (CFD). The hybrid set-up we are considering here can be also used in the study of flow induced by complex boundary conditions (such as rough surfaces) in nanotechnological processes, an active area of research with important applications in micro electromechanical systems (MEMS). For instance, Stroock *et al.* [7] showed that bas-relief nano-structures can be introduced on the floor of a slot in order to induce the mixing of solutions in low Reynolds number flows in microchannels.

Another objective of the present work is to study the effect of the microscopic fluctuations on the spatial and temporal resolution of the overall coupling scheme. To that end we quantify and analyze the averaging procedure needed in the particle measurements in order to achieve a given signal-to-noise ratio. Finally, we consider the velocity discontinuities that arise at the particle-continuum interface. We show that these can be controlled by using a hybrid velocity gradient in the imposition of the momentum flux on the continuum system at the particle-continuum interface. The idea of using hybrid gradients was first proposed by Flekkøy and Wagner in work addressing the hybrid description of the density field in Fickian diffusion [8].

The rest of the paper is organized as follows. In Sec II we present the domain decomposition used in our model, give details on the molecular domain and provide definitions of the spatial and time averages used in this work. In Sec. III we present the hybrid finite volume method used to inject the averaged microscopic flux into the continuum domain. The protocol for the C→P coupling is explained in Sec. IV. The hybrid scheme produces a finite signal-to-noise ratio due to the fluctuation of the particle momentum flux and, in Sec. V, we discuss how to use averaging procedures to maximize it. In Sec VI we apply the hybrid scheme to compute oscillatory shear flow in nanochannels. We also present some hybrid simulations to verify the conclusions of Sec. V concerning the rôle of fluctuations. Concluding remarks are given in Sec. VII.

## II. THE MOLECULAR REGION

A typical spatial domain decomposition for our hybrid scheme is depicted in Fig. 1. In the present set-up the overall domain ranges from  $x = 0$  to  $x = L_x$  and from  $-[L_\alpha/2, L_\alpha/2]$  in the other two periodic directions ( $\alpha = \{y, z\}$ ). The particle region (P) spans from  $x = 0$  to  $x = x_{CP}$ , the continuum region (C) from  $x = x_{PC}$  to  $x = L_x$  and both subdomains overlap within  $x_{PC} \leq x \leq x_{CP}$ .

The particle region (P) contains  $N(t)$  particles at time  $t$ , interacting through interparticle potentials and evolving in time through Newtonian dynamics. In this work, the particles interact through a truncated Lennard-Jones (LJ) potential  $\psi(r) = \psi_{LJ}(r) - \psi_{LJ}(r_o)$  where  $\psi_{LJ}(r) = 4\epsilon^{-1} [(\sigma/r)^{12} - (\sigma/r)^6]$ . Simulations were performed for the purely repulsive WCA Lennard-Jones potential [9] using a cut-off radius of  $r_o = 2^{1/6}\sigma$  and for the standard LJ fluid using a larger cut-off radius  $r_o = 3\sigma$ .

Each particle has a mass  $m$ , velocity  $\mathbf{v}_i$  and energy  $\epsilon_i = \frac{1}{2}mv_i^2 + \sum_j \psi(r_{ij})$  ( $\mathbf{r}_{ij} = \mathbf{r}_j - \mathbf{r}_i$ ). The equations of motion for the particles are

$$\dot{\mathbf{r}}_i = \mathbf{v}_i \tag{1}$$

$$\dot{\mathbf{v}}_i = \mathbf{f}_i = \sum_{i < j}^{N(t)} r_{ij}^{-1} d\psi(r_{ij})/dr_{ij} \mathbf{r}_{ij}, \quad (2)$$

where  $\mathbf{f}_i$  is the force acting on the  $i^{\text{th}}$  particle. Equations (1) and (2) were solved via standard molecular dynamics (MD) using the velocity-Verlet algorithm [10] with a time step  $\Delta t_P \simeq 10^{-3}\tau$ , where  $\tau = (m\sigma^2/\epsilon)^{1/2}$  is the characteristic time of the LJ potential. Throughout the rest of the paper, all quantities will be expressed in reduced units of the LJ potential:  $\tau (= 0.45 \times 10^{-13}\text{s})$ ,  $\sigma (= 3.305 \times 10^{-12}\text{cm})$ ,  $\epsilon$ ,  $m (= 6.63 \times 10^{-23}\text{g})$  and  $\epsilon/k_B (= 119.18\text{K})$  for time, length, energy, mass and temperature respectively (the numerical values correspond to argon).

The particle system is bounded in the  $x$  direction by a lower wall located at  $x = 0$  which contains a layer of 1600 spheres strongly tethered to the sites of the (1, 1, 1) plane of an fcc lattice by harmonic springs of stiffness  $\kappa = 1320\epsilon\sigma^{-2}$ . The wall atoms do not interact with each other and the wall-fluid interaction is LJ with an increased cutoff and potential well,  $r_{o,w} = 1.311\sigma$  and  $\epsilon_w = 1.303$ . These values ensure vanishingly small slip velocities for the shear rates considered here.

In order to maintain the temperature of the system constant we used either a Nosé-Hoover thermostat [11] for the LJ fluid, or a Langevin thermostat [11, 12] for the WCA-LJ fluid. The local kinetic temperature, needed for the Nosé-Hoover thermostat, was calculated from the peculiar velocities within slices of width  $1.0\sigma$  along the  $x$  direction. Also, to ensure that the Langevin thermostat does not bias the shear profile, the Gaussian white noise and damping terms are only added to the equations of motion for the velocity components normal to the mean flow, the  $x$  and  $z$  directions [12]. Both thermostats proved to be equally efficient.

The coupling scheme is a two-fold communication between C and P, as can be understood from Fig. 1. Within the C→P domain, the fluxes evaluated from the continuum solution are imposed on the particle dynamics. This part of the coupling scheme has been discussed by Delgado-Buscalioni and Coveney [3] for the general scenario of mass, momentum and energy transfer in unsteady relaxing flows. On the other hand, the flux due to the particle dynamics across the P→C interface is to be injected into the continuum system as flux boundary conditions. In order to coherently communicate information between both descriptions of matter, the fluxes arising from the particle system must be averaged in time and space prior to transferring to the coarse-grained level. Moreover these averages need to be local on the coarse-grained coordinates and on the time scale of the C domain. To that end, around each coarse-grained spatial coordinate,  $\mathbf{R}$ , we define a cell of volume  $V(\mathbf{R})$  and, for any particle variable, say  $\phi(\mathbf{r}_i, t)$ , we define the local mean  $\Phi(\mathbf{R}, t)$  at the coarse grained location  $\mathbf{R}$  as

$$\Phi(\mathbf{R}, t) = \frac{\int_{V(\mathbf{R})} \sum_{i=1}^N \phi(\mathbf{r}_i, t) \delta(\mathbf{r} - \mathbf{r}_i) d^3\mathbf{r}}{\int_{V(\mathbf{R})} \sum_{i=1}^N \delta(\mathbf{r} - \mathbf{r}_i) d^3\mathbf{r}}, \quad (3)$$

where the integration is performed over the cell volume  $V(\mathbf{R})$  and the summation runs over the particle index. The corresponding spatio-temporal average is also local in the ‘‘coarse-grained’’ time  $t_C$  with a time averaging window of length  $\Delta t_{av}$ ,

$$\langle \Phi \rangle(\mathbf{R}, t_C) = \frac{1}{\Delta t_{av}} \int_{t_C - \Delta t_{av}}^{t_C} \Phi(\mathbf{R}, t) \delta(t - t_k) dt. \quad (4)$$

For the temporal average a number of samples  $n_s$  of the microscopic quantity are taken along the time interval  $\Delta t_{av}$  at times given by  $t_k = t_C - \Delta t_{av} + k\delta t_s$  ( $k = \{1, \dots, n_s\}$ ). To ensure statistically independent measurements the time interval between samples  $\delta t_s$  cannot be smaller than the decorrelation time of  $\Phi$ , which can be calculated from  $\int_0^\infty \langle \Phi'(t) \Phi'(0) \rangle dt / \langle (\Phi')^2 \rangle$ , where  $\Phi' \equiv \Phi - \langle \Phi \rangle$  (see Sec. V).

As shown in Sec. III, the average defined by Eqs. (3) and (4) is used within the P→C cell to evaluate the coarse-grained momentum flux from the particle region to the continuum domain. In this case the spatial average is computed within the volume  $V_{PC} \equiv V(\mathbf{R}_{PC})$ , where  $\mathbf{R}_{PC}$  is the location of the P→C cell. This average shall be denoted  $\langle \Phi \rangle_{PC}(t) \equiv \langle \Phi \rangle(\mathbf{R}_{PC}, t)$ . We shall focus on the P→C coupling of the shear stress. At any given time instant, the time-averaged mean momentum flux tensor evaluated within the P→C cell is given by

$$\langle \mathbf{j}_P \rangle = \frac{1}{V_{PC}} \left\langle \sum_{i=1}^{N_{PC}} m \mathbf{v}_i \mathbf{v}_i - \frac{1}{2} \sum_{i,j}^{N_{PC}} \mathbf{r}_{ij} \mathbf{F}_{ij} \right\rangle \cdot \mathbf{n}_{PC}, \quad (5)$$

where  $N_{PC}$  is the number of particles inside the P→C cell,  $\rho_{PC} = N_{PC}/V_{PC}$ , and  $\mathbf{n}_{PC}$  is the surface vector of the cell pointing toward the neighbouring C-region (see Fig. 1b).

### III. CONTINUUM DESCRIPTION AND P→C COUPLING

Within the C region the relevant variables are the macroscopic local densities associated with the conserved quantities. If  $\Phi$  is any conserved quantity (per unit mass), its conservation law is given by

$$\frac{\partial \rho \Phi}{\partial t} = -\nabla \cdot \mathbf{J}_\Phi, \quad (6)$$

In this work we shall consider isothermal fluids and restrict ourselves to the momentum density  $\rho \mathbf{u}(\mathbf{r}, t)$ . In what follows, the continuum velocity will be denoted by  $\mathbf{u}$  while  $\langle \mathbf{v} \rangle$  stands for the mean particle velocity. The flux of momentum is given by  $\mathbf{J}_\mathbf{u} = \rho \mathbf{u} \mathbf{u} + \mathbf{\Pi}$ , where the pressure tensor  $\mathbf{\Pi} = P \mathbf{1} + \boldsymbol{\tau}$  includes the local hydrostatic pressure  $P$  and the viscous stress tensor. For an LJ fluid, the latter satisfies a Newtonian constitutive relation [13, 14],  $\boldsymbol{\tau} = -\eta (\nabla \mathbf{u} + \nabla \mathbf{u}^T) + (2\eta/3 - \xi) \nabla \cdot \mathbf{u}$ , where  $\eta$  is the shear viscosity and  $\xi$  the bulk viscosity. In principle, the set of equations given by Eq.(6) can be solved by any standard continuum fluid dynamics (CFD) method. Nevertheless, as the hybrid scheme proposed here is based on the balance of fluxes it fits naturally with the finite volume method [15], which exactly balances the fluxes across the computational cells.

In order to illustrate the P→C coupling protocol we shall consider the flow of an incompressible and isothermal fluid with mean density  $\rho_c$  and mean temperature  $T_c$ . The fluid fills the space between two parallel walls at  $x = 0$  and  $x = L_x$ . The wall at  $x = L_x$  is moving with arbitrary velocity  $u_{wall}(t)$  along the  $y$  direction. The flow is uniquely driven by the motion of this wall, meaning that the mean pressure is constant throughout the domain,  $P = P_c(\rho_c, T_c)$ , and that there are no transfers of mean energy or mass along the  $x$  direction (perpendicular to the P→C interface). As discussed by Vogel *et al.* [16], if the system is not confined in the flow direction (as happens to be the case in our system) this flow is laminar and the velocity of the continuum flow is given by  $\mathbf{u} = u_y(x, t) \mathbf{j}$ . The stress tensor is  $\mathbf{J}_\mathbf{u} = P_c \mathbf{1} - \eta \partial u_y / \partial x \mathbf{j}$ . In the case of the LJ fluid, the value of the dynamic viscosity  $\eta$  was obtained from Heyes [14] and for the WCA-LJ fluid  $\eta$  was measured from MD simulations using a standard non-equilibrium procedure [17], i.e., from the ratio of the shear stress and shear rate in Couette flow. The equation of motion for the  $y$ -momentum is given by the unsteady diffusion equation

$$\frac{\partial u_y}{\partial t} = \nu \frac{\partial^2 u_y}{\partial x^2}, \quad (7)$$

where  $\nu = \eta / \rho_c$  is the kinematic viscosity. At the fixed wall, the boundary condition is  $u_y(0, t) = 0$  and at the moving wall  $u_y(L_x, t) = u_{wall}(t)$ .

For the finite volume discretization of Eq. (7) in the geometry of Fig. 1 we divide the extent of the C region along the  $x$ -coordinate ( $x_{PC} \leq x \leq L_x$ ) into  $M$  cells. The faces of the cells can be placed at arbitrary positions  $x_k^f$  with  $k = \{0, \dots, M\}$ , and the centres of the cells at  $x_k = (x_k^f + x_{k-1}^f) / 2$  with  $k \in \{1, \dots, M\}$ . To derive a closed set of equations for the velocities  $u_y(x_k)$  at the  $k \in \{1, \dots, M\}$  cell centres, one integrates Eq. (7) over the volume of each cell. For a given cell, say  $k = H$ , the integration is done over  $x^w \leq x \leq x^e$ , where the cell faces of the  $H$  cell ( $x^w$  and  $x^e$ ) are illustrated in Fig. 1b. The resulting first order spatial derivatives at the cell faces  $x^e$  and  $x^w$  are discretized as, e.g.,  $\partial u_y(x^e) / \partial x = (u_y(x_E) - u_y(x_H)) / (x_E - x_H)$ ; where the ‘‘east’’ cell  $E = H + 1$  is placed at  $x_E = x_{H+1}$  and the ‘‘west’’ cell  $W$  at  $x_W = x_{H-1}$ . We use an explicit time integration scheme by approximating the time derivative at the centre of the cell by  $\partial u_y / \partial t \simeq (u_y(t + \Delta t_C) - u_y(t)) / \Delta t_C$ , where  $\Delta t_C$  is the time step. We refer to the excellent book of Patankar [15] for a comprehensive presentation of the finite volume discretization of Eq. (7) and Navier-Stokes equations including a discussion on the different time integration schemes. The resulting discretized version of equation (7) reads,

$$u_y(x_H, t + \Delta t_C) = (1 - r_e - r_w) u_y(x_H, t) + r_e u_y(x_E, t) + r_w u_y(x_W, t), \quad (8)$$

with  $E = H + 1$ ,  $W = H - 1$  and  $H = \{1, \dots, M\}$ .

We have introduced  $r_e$  and  $r_w$ , defined as  $r_f \equiv \nu \Delta t / (\Delta x^f \Delta x_H)$  where  $f = \{w, e\}$ ,  $\Delta x^f$  is the the centre-to-centre distance and  $\Delta x_H$  the face-to-face distance, as shown in Fig. 1b. Most of the simulations reported in this work were performed with a regular grid [31] ( $r \equiv r_w = r_e$ ), using  $\Delta x \sim 0.5$ . The time step  $\Delta t_C$  was chosen to fulfil the Courant condition  $r \leq 1/2$ , which ensures the stability of the explicit scheme in Eq. (8) [15]. Note that Eq. (8) is not closed for the velocities at the  $H = \{1, \dots, M\}$  cell centres. For instance, the evaluation of the velocity at the cell  $H = M$  requires the velocity at the outer cell  $E = M + 1$ , which is outside the computational domain of the C region. Similarly, for the velocity at  $H = 1$  one requires the velocity at the outer cell  $W = 0$ . The velocities at these outer cells (also called *ghost* cells) have to be evaluated from the boundary conditions. For instance, the velocity of the *ghost* cell  $E = M + 1$  at  $x_{M+1} = L_x + \Delta x_E / 2$  is calculated by linear extrapolation from the velocity at the  $H = M$  cell and the velocity at the wall:  $u_y(x_E, t) = u_y(x_H, t) + 2\Delta x^e (u_{wall}(t) - u_y(x_H, t)) / \Delta x_H$ , where  $H = M$ .

In the same way, to close Eq. (8) for  $H = 1$  we need to determine the velocity at the *ghost* cell  $W = 0$  at  $x_0 = x_{PC} - \Delta x_W/2$ . To that end we use the hybrid formulation and set the  $y$ -momentum flux across P→C equal to the time-averaged momentum flux due to the particle system at the P→C cell:  $\langle j_{p,xy} \rangle_{PC} = -\eta(\partial u_y/\partial x)_{x_{PC}}$ . The discretized version of the right hand side (RHS) of this momentum flux balance equation is expressed as  $-\eta(\bar{u}_y(x_H) - u_y(x_W))/\Delta x^w$ , with  $H = 1$  and  $W = 0$ . Note that both the particle and the continuum domains overlap at the first cell  $H = 1$ , so the velocity  $\bar{u}_y(x_H)$  could be chosen to be either the time averaged mean particle velocity at the  $H = 1$  cell,  $\langle v_y \rangle(x_H)$  or the continuum velocity at the same location,  $u_y(x_H)$ . The implication of such a choice will become clear shortly. We have enabled a set of possible choices based on a linear combination of both velocities,

$$\bar{u}_y(x_H) = (1 - \alpha)u_y(x_H) + \alpha\langle v_y \rangle(x_H), \quad \text{for } H = 1 \text{ and } \alpha \in [0, 1]. \quad (9)$$

The flux balance equation  $\langle j_{p,xy} \rangle_{PC} = -\eta(\bar{u}_y(x_H) - u_y(x_W))/\Delta x^w$  provides the velocity at the ghost cell  $u_y(x_W)$ , required to close Eq. (8) for  $H = 1$ ,

$$u_y(x_W) = \bar{u}_y(x_H) + \langle j_{p,xy} \rangle_{PC} \Delta x^w / \eta \quad \text{for } W = 0 \text{ and } H = 1. \quad (10)$$

Insertion of Eq. (10) and Eq. (9) into Eq. (8) provides the time advancement algorithm for the velocity at the cell interfacing the particle system:

$$\begin{aligned} u_y(x_H, t + \Delta t_C) = & (1 - r_e) u_y(x_H, t) + r_e u_y(x_E, t) + \frac{\langle j_{p,xy} \rangle_{PC}(t) \Delta t}{\rho \Delta x^w} + \\ & + \alpha r_w (\langle v_y \rangle(x_H, t) - u_y(x_H, t)), \quad \text{for } H = 1, E = 2. \end{aligned} \quad (11)$$

The effect of the choice of  $\alpha$  in Eq. (9) becomes clear by inspection of Eq. (11). For any  $\alpha \neq 0$  the last term on the RHS of Eq. (11) acts as a relaxation term that ensures velocity continuity by gently driving the continuum velocity at the boundary cell  $x = x_1$  to the corresponding particle average  $\langle v_y \rangle(x_1)$ . This term vanishes or becomes negligible once velocity continuity is established,  $u_y(x_1) \simeq \langle v_y \rangle(x_1)$ . We emphasise that this sort of *velocity coupling* does not directly act on the particle dynamics, but only within the algorithm for the continuum dynamics. This fact is significant because it avoids any artificial alteration (such as a Maxwell dæmon) to the microscopic dynamics of the particles near the P→C interface. The idea of using the scheme in Eq. (11) arose from the outcome of calculations performed at low shear rates for which  $du_y/dx < 10^{-2}$ . At low shear rates the velocity fluctuations become significant enough to produce deviations of the mean particle and continuum velocities at the overlapping region. If the velocity coupling term is absent in Eq. (11) ( $\alpha = 0$ ) the deviations of the P and C velocities produced by subsequent particle fluctuations can be maintained in time, although the slopes of the P and C velocities do converge to the same value (see Figs. 2, 3 and discussion below). The reason for this fact is clear: the imposition of a flux does not prescribe the value of the velocity, but only its gradient. As shown below, the algorithm in Eq. (11) solves the problem of velocity continuity even when a small velocity coupling is used  $\alpha$  ( $\sim 0.1$ ).

To demonstrate the effect of the parameter  $\alpha$  in Eq. (11) on velocity continuity we performed some hybrid simulations of Couette flow using a Lennard-Jones fluid with density  $\rho = 0.8$  and temperature and  $T = 1.0$ . Similar tests were also done in the simulations of oscillatory shear flow presented in Sec VI. These tests were performed with  $\alpha = \{0, 0.1, 0.2, 1\}$ . Figure 2 shows the  $y$ -velocity profile of a Couette flow with  $du_y/dx = 0.01724$ , obtained by averaging within slices of width  $0.2\sigma$  and over the whole simulation time. Results obtained for  $\alpha > 0$  do not present any velocity discontinuity and are in perfect agreement with the analytical profile (the local shear rate at the  $x_{CP}$  interface deviates by less than 2% from  $u_{wall}/L_x$ ). On the contrary, when using  $\alpha = 0$  in Eq. (11), the averaged velocity profile presents a significant discontinuity at the overlapping region which affects the overall shear rate of the flow. As shown in Fig. 2 the discontinuity tends to be reduced as the average time is increased, but it is still significant after an average time over  $1500\tau$ .

The effect of the parameter  $\alpha$  in the continuity of velocity is more clearly shown in Fig. 3 where the continuum and mean particle velocities at the boundary cell  $H = 1$  are plotted *versus* time. Using  $\alpha = 1$  the relative differences between the C and P velocities are less than 2%, while for a value of  $\alpha$  as small as 0.2, these relative differences are still less than 5%. By contrast, when using  $\alpha = 0$ , this relative difference increases to  $\sim 80\%$ . As seen in Fig. 3, for  $\alpha = 0$  the C velocity and averaged P velocity at the cell  $H = 1$  “oscillate” around the correct value  $\sim 0.28$ , and the period of these oscillations can be as large as  $\sim 600\tau$ . For smaller shear rates the situation worsens because this period may become much larger. In summary, using  $\alpha = 0$  the numerical scheme of Eq. (11) does not guarantee velocity continuity. Inspection of Fig. 3a clearly indicates that using  $\alpha > 0$  enables us to deal with time-dependent flows, as shown in Sec. VI.

The central idea of our hybrid scheme is the balance of fluxes and such a balance must to be respected by any choice of  $\alpha$ . To investigate this we compared the time averaged flux injected from the particle system with the time averaged flux measured from the continuum field at the interfacing cell,  $H = 1$ . If the flux exchange is correctly balanced, both

$\alpha$	Particle system		Continuum system	
	$\langle j_{p,xy} \rangle_{PC}$	$S_{j_p}$	$\Pi_{xy}(x_{PC})$	$S_{\Pi}$
0	0.0289	0.09	0.0294	0.01
0.2	0.0287	0.08	0.0294	0.01
1	0.0298	0.08	0.0297	0.01

TABLE I: The fluxes across the P→C interface for different values of the  $\alpha$  parameter. Comparison is made between the time averaged particle flux  $\langle j_{p,xy} \rangle$  and the time averaged momentum flux in the continuum field,  $\Pi_{xy}(x_{PC}) \equiv -\eta(du_y/dx)_{PC}$ . Time averages were performed over  $\sim 1000\tau$ . The results were obtained from a Couette flow with imposed shear rate  $u_{wall}/L_x = 0.0172$  (see Fig. 2). The momentum flux measured from the C flow is calculated using  $\eta = 1.75 \pm 0.05$  and a discretized version of the velocity gradient near the P→C interface,  $du_y/dx = (u(x_2) - u(x_1))/\Delta x$  (where  $x_1 = x_{PC} + \Delta x/2$ ,  $x_i = x_1 + i\Delta x$  and  $\Delta x = 0.9$  is the width of the spatial mesh). For all values of  $\alpha$  the time averaged P and C-fluxes coincide well within their fluctuation margins and agree with the externally imposed stress,  $\eta u_{wall}/L_x = 0.030 \pm 0.001$ . The amplitude of the fluctuations of both fluxes (their standard deviation) has been also indicated by  $S_j$  and  $S_{\Pi}$ . All quantities are expressed in LJ reduced units  $m\sigma^{-1}\tau^{-2}$ .

quantities should coincide. The outcome of these tests is shown in Table 1. For any  $\alpha \in [0, 1]$ , both fluxes differ by less than 2% indicating that the velocity coupling term in Eq. (11) does not alter the balance of fluxes.

We note that the velocity coupling term in Eq. (11) introduces an extra momentum flux into the C system whose magnitude is  $\alpha\eta(\langle v_y \rangle(x_H, t) - u_y(x_H, t))/\Delta x$ . This flux fluctuates on the microscopic time scale and its average is close to zero. This fact explains why the relaxing term does not affect the flux balance on the time scale of the coarse-grained dynamics, as can be seen in Table 1. We measured the relative size of the flux contributions in Eq. (11) and concluded that the size of the relaxing term remains much smaller than the particle flux for shear rates larger than  $\gamma > 10^{-3}$ . Below a certain shear rate,  $\gamma \sim 10^{-3}$ , the fluctuations of the relaxing term are of the same order as the particle flux signal. Nevertheless, for such small shear rates the signal-to-noise ratio of the particle flux becomes larger than one (see Sec. V) and we are obliged to perform temporal averages over long times to recover the correct velocity profile and flux balance. We performed simulations of a Couette flow at  $\gamma = 10^{-3}$  using  $\alpha = 0.5$ . The values of the fluxes, averaged over a time of  $10^4\tau$ , were  $\langle j_{p,xy} \rangle_{PC} = (1.9 \pm 2.1) \times 10^{-3}$  while  $-\eta(du_y/dx)_{PC} = (1.8 \pm 0.3) \times 10^{-3}$  (here the error bars denote half the standard deviation). These values compare well with the externally imposed stress,  $\eta u_{wall}/L_x = (1.75 \pm 0.05) \times 10^{-3}$ . In passing, we note that owing to the effect of the strong fluctuations, when simulating flows with  $\gamma \sim 10^{-3}$  using  $\alpha = 0$ , the averaged P and C velocities in the handshaking region never matched; hence, although the fluxes (and therefore the velocity gradients) were perfectly balanced, they did not agree with the desired, externally imposed, value.

One might ask what value of  $\alpha \neq 0$  is best suited for a certain simulation. We give here indications as to how to answer this question. Note that the velocity coupling takes a characteristic relaxation time  $O[\Delta x^2/(\nu\alpha)]$  to drive the continuum velocity towards the average particle velocity. As stated above this time can be very short, for instance in simulations with  $\alpha = 1$ ,  $\Delta x \sim 1$  and  $\nu \sim 2.0$ , one finds a relaxation time  $\sim 1\tau$  which lies within the characteristic time of the microscopic fluctuating currents [3]. In flows where the amplitude of particle fluctuations is expected to be large (e.g. at very low shear rates or near the critical point) it may be desirable to increase this relaxation time by using a smaller value of  $\alpha \sim 0.1$ . In this way one can prevent large jumps in the continuum velocity which may lead to numerical instabilities of the CFD algorithm for the continuum domain.

#### IV. THE C→P COUPLING: CONTROL OF MASS FLUCTUATIONS

For a detailed description of this part of the hybrid scheme we refer to Delgado-Buscalioni and Coveney [3], where the C→P protocol is applied to the general scenario of flows with time-dependent mass, transversal and momentum and energy transfers. For completeness we now briefly explain how the momentum flux from the C flow is injected into the particle system. We also present a way to control the fluctuations of mass across the C→P interface so as to ensure the balance of mass flux.

##### A. Imposition of the shear stress on the particle system

This part of the coupling scheme occurs within the C→P cell shown in Fig. 1a. The stress induced by the C-flow in the P domain is given by the local momentum flux at the C→P interface at  $x = x_{CP}$ . The flow considered here only carries transversal momentum (i.e. along the  $y$ -direction), so the momentum flux is given by

$$\mathbf{\Pi}_{CP} \cdot \mathbf{n}_{CP} = -P_c \mathbf{i} + \eta(\partial u_y/\partial x)_{x_{CP}} \mathbf{j}, \quad (12)$$

where  $\mathbf{n}_{CP} = -\mathbf{i}$  is the surface vector of the C→P interface. In order to introduce this stress into the particle dynamics we add an overall external force  $\mathbf{F}_{\text{ext}} = A\mathbf{\Pi}_{CP} \cdot \mathbf{n}_{CP}$  to those particles within the C→P cell. For any instant of time,  $t$ , this force is equally distributed among the  $N_{CP}(t)$  particles inside the C→P cell, so the external force per particle is  $\mathbf{F}_{\text{ext}}/N_{PC} = A\mathbf{\Pi}_{CP} \cdot \mathbf{n}_{CP}/N_{CP}$ . Note that this external force has a component normal to the C→P interface, which provides the hydrostatic pressure, and a tangential component providing the shear stress. The particles are free to enter or leave the C→P region, so the number of particles within this region  $N_{CP}(t)$  and the value of the overall external force fluctuate in time. The mean value of  $N_{CP}$  is  $A\Delta x_{CP}\rho_{CP}$  so the average “pressure force” per particle is  $P_c/(\Delta x_{CP}A^2\rho_{CP})$ , where  $\Delta x_{CP} \simeq 2\sigma$  is the extent of the C→P cell along the  $x$  direction,  $A = L_y \times L_z$ , the local density is  $\rho_{CP} = N_{CP}/V_{CP}$ , and the pressure  $P_c(\rho_c, T_c)$  is given from the equation of state which in the case of the WCA-LJ fluid was provided by Hess *et al.* [9] and for the standard LJ fluid by Johnson *et al* [18]. This normal force prevents the escape of particles and maintains the correct value of the density across the inner part of the MD domain as seen in Fig. 4. The shear force is distributed over the particles in the same way as described above for the pressure force. In this case, the flux of  $y$ -momentum to be injected in the particle system is  $\eta(\partial u_y/\partial x)_{x_{CP}}$ .

### B. Control of mass fluctuations across the C→P interface

For the flows we are treating here, the mean fluxes of mass and energy across the C and P interfaces are zero but fluctuations in the particle system produce perturbative mass currents along the  $x$  direction which need to be controlled. For this purpose, we coupled the end region of the P domain with a control equation that governs the mass flux across the particle system frontier. This control equation is derived using the finite volume rationale: we integrate the mass conservation equation  $\partial\rho/\partial t = -\nabla(\rho\mathbf{u})$  in a control volume around the C→P interface (between  $x_{CP} = x_{CP} - \Delta x_{CP}/2$  and  $x_O \equiv x_{CP} + \Delta x_{CP}/2$ ) to obtain the particle flux towards the C domain. Zero mass flux is ensured by equating this rate to the rate of insertion in the particle system,  $\dot{N}_{PC}$ . This yields

$$\dot{N}_{CP} = A(\langle\rho v_x\rangle_{CP} - \rho_c u_x(x_0)) = A\langle\rho v_x\rangle_{CP}, \quad (13)$$

where  $\dot{N}_{CP}$  is the time derivative of the number of particles within the C→P cell. The mean particle mass flux  $\langle\rho v_x\rangle_{CP}$  is evaluated within the C→P cell and averaged over  $\Delta t_{av}$ . On the right hand side of Eq. (13) we have used the fact that the normal velocity in the C domain is zero,  $u_x(x_0) = 0$ . Equation (13) proved to be successful in ensuring mean zero mass flux and in eliminating any incoming longitudinal mass currents towards the C→P interface.

We also used a different strategy to fix the rate of particle insertion/removal, which provides further control on the particle density near the C→P interface. In this second approach the particle insertion rate is chosen to make the particle number in the C→P cell  $\rho_{CP}$  relax to a pre-set value  $\rho_O$ ,

$$\dot{N}_{CP} = \frac{V_{PC}}{\tau_r} (\langle\rho\rangle_{CP} - \rho_O), \quad (14)$$

where  $V_{PC}$  is the volume of the C→P cell and  $\tau_r$  is a relaxation time. As before,  $\langle.\rangle$  denotes the time average over  $\Delta t_{av}$ . The amplitude of the density fluctuations within the C→P cell is controlled by the coefficient  $\tau_r$  and can be chosen according to the requirements of the problem. For instance, in hybrid simulations of tethered polymers under Couette flow [19] one may need to smooth out the perturbative density waves originated by the tumbling motion of the polymer at the inner part of the MD domain. Otherwise these waves can bounce back at the C→P interface and affect the dynamics of the polymer. To that end, the relaxation time  $\tau_r$  need to be smaller than the time needed for a sound wave to cross the width of the C→P buffer,  $\Delta x_{CP}/c_s$ , where  $c_s$  is the sound velocity (see e.g. [3]). The procedure implemented according to Eq. (14) is an artifact that ensures fluctuations carrying mass and longitudinal currents are filtered out from the simulation box. In problems where the pressure waves are an essential part of the study, the mass flux will be governed by the longitudinal momentum and energy equations, which will need to be added into the hybrid formalism. According to Eq. (14), particles are extracted if  $\dot{N}_{PC} < 0$  and, as explained in Ref. [3], the first particles to be extracted are those closest to the C→P interface. If  $\dot{N}_{PC} > 0$ , new particles are inserted with a velocity extracted from a Maxwellian distribution with mean velocity and temperature given by the continuum values  $\mathbf{u}(x_{CP})$  and  $T = T_c$ . The insertion of particles in dense fluids is a far from trivial task but it has been solved by the USHER algorithm proposed by Delgado-Buscalioni and Coveney [20].

The value of  $\rho_O$  in Eq.(14) was set to a slightly smaller value than the mean density. The reason for this choice was first to alleviate the computational cost of insertion [32] and second to reduce the amplitude of ripples of the density profile near the C→P buffer. For a fluid with  $\rho_c = 0.8$ , we compared the density profile arising from a full MD simulation with that resulting using  $\rho_O = 0.7$  and  $\rho_O = 0.5$  in Eq. (14). This comparison is shown in Fig. 4. For both values of  $\rho_O$ , the “hybrid” density profile presents some ripples near the C→P cell which are damped after around  $3\sigma$ . Within the P→C cell the hybrid density profile perfectly matches the density within the bulk.

We also estimated the cost in CPU time of the USHER algorithm for the particle insertion (see Ref. [19] for further details). As an example, in a fluid with  $\rho_c = 0.8$ , using  $\rho_O = 0.7$  in Eq. (14), a total number of particles of  $\sim 10^4$  and an overall simulation CPU time of 20000 seconds, the CPU time spent within the particle insertion/extraction subroutine was about 0.003 times the CPU time used by the main force subroutine of the MD code used in this study (which uses the Verlet list for counting neighbouring particles [10]). This excellent performance indicates that the USHER scheme is well suited for the insertion protocol in the hybrid scheme when using Lennard-Jones particles as the fluid of interest.

## V. SHEAR STRESS FLUCTUATIONS AND ACCURACY LIMITS

In our scheme, the fluctuating nature of the fluxes introduced into the C region from P→C imposes a limitation on our ability to resolve the flow field, as also arises in experiments and full MD simulations. This limit is determined by the signal-to-noise ratio becoming smaller than one. We shall now consider the effect of fluctuations of the transversal momentum flux and provide an estimation of its signal-to-noise ratio in order to derive the resolution limit of the hybrid scheme. This task requires consideration of the autocorrelation of the transversal momentum flux or, in other words, of the  $xy$  component of the microscopic stress tensor defined in Eq. (5)

$$G(t) = \frac{V_{PC}}{T} \langle j'_{p,xy}(t) j'_{p,xy}(0) \rangle_{st}, \quad (15)$$

where  $\langle \cdot \rangle_{st}$  denotes the statistical ensemble average (assuming ergodicity, we measured it by performing the time average over a long enough simulation time) and  $j'_{p,xy} = j_{p,xy} - \langle j_{p,xy} \rangle_{st}$ . Equation (15) gives a direct relationship between the amplitude of the stress tensor fluctuations and the shear modulus  $G(0)$

$$\langle (j'_{p,xy})^2 \rangle_{st} = \frac{T}{V_{PC}} G(0). \quad (16)$$

In the case of a LJ fluid the shear modulus is known and is given by  $G(0) = 3P - \frac{24}{5}\rho U - 2\rho T$  [21, 22]. For other interatomic potentials the route described above would require the evaluation of  $G(0)$  from MD simulations since the algebraic relationship of  $G(0)$  with thermodynamic variables is not normally available.

To evaluate the size of the stress tensor fluctuations we shall use an equivalent route involving the transport coefficient (shear viscosity) and the corresponding Green-Kubo relation

$$\eta = \int_0^\infty G(t) dt. \quad (17)$$

Let us approximate  $G(t) \approx \eta \exp(-t/\tau_G)/\tau_G$ , where  $\tau_G$  is a decorrelation time which can be calculated from the outcome of a simulation by  $\tau_G = \int_0^\infty G(t) dt / G(0)$ . Using Eqs. (15)-(16) one obtains

$$\langle (j'_{p,xy})^2 \rangle_{st} = \frac{T\eta}{V_{PC}\tau_G}. \quad (18)$$

We note that  $\lim_{\tau_G \rightarrow 0} [\exp(-t/\tau_G)/\tau_G] = 2\delta(t)$ , where  $\delta(t)$  is the Dirac delta function. Hence the Landau expression for the fluctuation of the stress tensor  $\mathbf{\Pi}$  is coherently recovered from (18) in the limit of the delta correlated process,  $\tau_G \rightarrow 0$

$$\langle (\mathbf{\Pi}'_{xy})^2 \rangle_{st} = \frac{2T\eta}{V_{PC}} \delta(t). \quad (19)$$

The Landau expression [23] comes from a Langevin dynamics approach and is valid for a coarse-grained process in which the time step (or time between measurements) is much larger than the decorrelation time  $\tau_G$ .

Table 2 shows the amplitude of the fluctuations of the microscopic shear stress  $\langle (j'_{p,xy})^2 \rangle$  for several calculations of a Couette flow at very small shear rate  $\gamma \simeq 0.002$ . We confirmed that for these values of  $\gamma$  the variance of the shear stress and velocity are similar to their values at equilibrium. Results were obtained for both the LJ and the WCA fluid. The numerical results are in good agreement with the theoretical expression given in Eq. (18), where the decay time was measured from simulations,  $\tau_G \simeq 0.06$ . In the case of the LJ fluid (for which the value of  $G(0)$  is available) the values of  $\langle (j'_{p,xy})^2 \rangle$  obtained from Eq. (16) are compared with Eq. (18) in Table 2.

The standard deviation of the microscopic momentum flux averaged over a time interval  $\Delta t_{av} = n_s \delta t_s$  is given by  $S^2 = \langle (j'_{p,xy})^2 \rangle / n_s$ . We note that for this relation to hold the time interval between samples  $\delta t_s$  needs to be somewhat larger than  $\tau_G \simeq 0.06$ , in order to ensure a number  $n_s$  of statistically independent evaluations of  $j_{p,xy}$ .



Fluid	$V_{PC}$	$T$	$\eta$	Numerical $\langle (j'_{p,xy})^2 \rangle$	Theoretical $\langle (j'_{p,xy})^2 \rangle$
WCA	81	1	1.75	0.51	0.60
WCA	173	1	1.75	0.40	0.41
WCA	138	1	1.75	0.33	0.38
WCA	338	1	1.75	0.25	0.24
WCA	2778	1	1.75	0.08	0.06
WCA	2778	1	1.75	0.04	0.03
LJ	121.5	4.0	2.12	1.09	1.08 (1.19)
LJ	121.5	2.0	1.90	0.66	0.72 (0.71)
LJ	121.5	1.0	1.75	0.39	0.49 (0.43)

TABLE II: The variance of the microscopic momentum flux for  $\rho = 0.8$ . The theoretical results come from Eq. (18) using  $\tau_G = 0.06$ ; those in parentheses are derived from Eq. (16).

For the shear flows considered here the mean momentum flux can be expressed as  $\eta\gamma$  and the signal-to-noise ratio is  $E \equiv \eta\gamma/S$ . We now demand  $E > O(1)$  to obtain conditions on  $V_{PC}$  and  $\Delta t_{av}$ ; using Eq. (18) one obtains

$$E^2 = \frac{\gamma^2 \eta}{T} \frac{\tau_G}{\delta t_s} \Delta t_{av} V_{PC} > O(1) \quad (20)$$

and using  $\delta t_s \geq \tau_G$  one gets,

$$V_{PC} \Delta t_{av} > \frac{T}{\gamma^2 \eta}. \quad (21)$$

Equations (20) and (21) give some control over the amplitude of the fluctuations of the coarse-grained (space-time averaged) stress tensor. For instance, in the case of steady state flows the signal-to-noise ratio can be increased by enlarging  $V_{PC}$ ,  $\Delta t_{av}$ , or both. But if the flow is not homogeneous in space or if it is time-dependent,  $V_{PC}$  and  $\Delta t_{av}$  are bounded above by the requirement of spatial and temporal flow resolution. In other words, to resolve a flow whose shortest characteristic time is  $\omega_{\max}^{-1}$  and whose maximum wavenumber is  $k_{\max}$ , the temporal and spatial resolution conditions are  $\Delta t_{av} \omega_{\max}^{-1} \leq O(0.1)$  and  $\Delta x_{PC} k_{\max} \leq O(0.1)$ , where  $V_{PC} = A_{PC} \Delta x_{PC}$  (see Fig. 1). Inserting these conditions into Eq. (21) one gets that the range of frequencies and wavenumber that can be resolved is bounded above by  $k\omega < \gamma^2 \eta T^{-1} A_{PC}^{-2}$ .

## VI. APPLICATION TO OSCILLATORY SHEAR FLOW

In order to test the applicability of the full hybrid scheme under unsteady flows, we consider the flow of an incompressible and isothermal fluid between two parallel walls in relative oscillatory motion. In our test flow, the simulation domain is  $0 \leq x \leq L_x$  and it is periodic along  $y$  and  $z$  directions. The particle domain occupies the region  $x < l_P$ , and it includes the LJ liquid and the atomistic wall composed of two layers LJ particles at  $x \leq 0$ . The continuum domain comprises the region  $x \in [l_C, L_x]$ . The sizes of the simulation domains are within the nanoscale  $L_x \sim 50\sigma$ , and  $l_P \sim 15\sigma$ , while the width of the handshaking region are  $l_P - l_C \sim 5\sigma$ . The flow is uniquely driven by the oscillatory motion of the  $x = L_x$  wall along the  $y$  direction, meaning that the mean pressure is constant throughout the domain and there are no transfers of mean energy or mass in the  $x$  direction (perpendicular to the P→C surface). The mean flow carries transversal momentum by diffusion only, and the equation of motion for the  $y$ -velocity is  $\partial u / \partial t = \nu \partial^2 u / \partial x^2$ , with boundary conditions  $u(0, t) = 0$  and  $u(L, t) = u_{wall}(t) = u_{\max} \sin(\omega t)$ . This equation can be solved analytically [6, 24, 25]. The flow profile has a maximum amplitude at the moving wall and the momentum introduced by its motion penetrates into a fluid layer of width  $\delta \sim \sqrt{\pi\nu/f}$ . Beyond this layer (usually called the viscous layer) the flow amplitude tends to zero diffusively as it approaches the other wall held at rest. Therefore, the maximum shear rate attained inside or near the viscous layer is of order  $\gamma \sim u_{\max}/\delta$ . Inserting this relation into the signal-to-noise condition (21), we find

$$\rho u_{\max}^2 \Delta t_{av} > \pi f^{-1} \left( \frac{k_B T}{V_{PC}} \right), \quad (22)$$

which clearly means that in order to attain a signal-to-noise ratio  $E$  larger than one, the mean kinetic energy of the flow integrated over the averaging time  $\Delta t_{av}$  needs to be larger than the net energy due to fluctuations over a period of the mean flow. We note that at low enough frequencies,  $f > \nu/L^2$ , diffusion is the fastest process in the system (momentum has enough time to spread mass over the whole domain) and in such cases the correct condition to guarantee  $E < 1$  is given by Eq. (21), with  $\gamma \sim u_{\max}/L^2$ .

In order to resolve the temporal variation of the flow the averaging time has to be a fraction of the shorter characteristic time of the flow, which corresponds here to the period of the oscillation,  $f^{-1}$ . This condition,  $\Delta t_{av} f \geq O(0.1)$ , can be inserted into Eq. (22) to obtain an estimation of the range of wall velocities that the scheme can resolve:  $u_{\max} > 5 \left( \frac{k_B T}{\rho V_{PC}} \right)^{1/2}$ . For  $k_B T = 1.0$ ,  $\rho = 0.8$  and  $V_{PC} = O(100)$  the above inequality yields  $u_{\max} > 0.5$ . Provided that  $\Delta t_{av} f$  is fixed to a low value, we note that the former condition is independent of the external frequency because the shear stress is approximated by  $\gamma \sim u_{\max}/\delta$ . This is only valid up to the end of the viscous layer because  $\gamma = \gamma(x)$  becomes very small beyond this layer ( $x > \delta$ ). Also, using the analytical flow solution [6] it can be easily shown that for a fixed  $u_{\max}$ , the local shear rate within the viscous layer decreases slightly with the frequency. In fact, the characteristic Reynolds number of the flow goes like  $f^{-1/2}$ :  $Re^* = u_{\max} \delta / \nu \sim u_{\max} f^{-1/2} \nu^{-1/2}$ . As an aside, the flow considered here (the oscillatory shear flow in between infinite planes or stream-wise periodic boundary conditions) is linearly stable [16]. As shown in a recent paper, flow instabilities in the form of three-dimensional rolls do arise at  $Re \equiv u_{\max} L_x / \nu \simeq 500$  only if the zero mass-flux condition along the stream-wise direction is imposed by confinement of lateral walls [16]. The range of Reynolds number considered here was such that  $Re \leq 200$ .

In order to test the hybrid model and the above observations on the amplitude of fluctuations, we performed oscillatory shear simulations for values of  $u_{\max}$  above, near and below the threshold given by Eq. (22). In the following calculations the domain geometry is  $L_x = 30$  and in the periodic directions  $L_y = L_z$  were set to values between 6 and 9. Calculations for the large amplitude flow are in excellent agreement with the analytical solution as illustrated in Fig. 5, where  $u_{\max} = 10$ ,  $f = 0.01$ , and  $\Delta t_{av} = 1$ .

Figure 6 shows several snapshots of the velocity profiles in the case of a large amplitude flow ( $u_{\max} = 10$ ,  $f = 0.01$ ) of a LJ fluid at density 0.8 and temperature  $T = 1.0$ . The P region spreads from the atomic wall at  $x = 0$  to  $x = 15$  and the C region comprises  $x = [11.8, 30]$ . The centres of the P→C and C→P cells were set 3.2 apart and their width was 1.6. The outcome of the hybrid simulation is in very good agreement with the analytical solution, plotted in dashed lines.

The calculations shown in Fig. 6 were performed for a velocity coupling of  $\alpha = 0.5$ . Figure 7 compares this result with another calculation using  $\alpha = 0$ . In the latter case, discontinuities of velocity are clearly observed within the overlapping region, its maximum size, around 0.35, being consistent with the size of the velocity (and momentum flux) fluctuations within the overlapping region. It is interesting to note that such discontinuities can be smoothed out by using values of  $\alpha$  as small as 0.2. In other words, the model is not very sensitive to the actual value of  $\alpha$ , provided  $\alpha > 0$ .

Some simulations with the same fluid (LJ at  $\rho = 0.8$  and  $T = 1$ ) but using a smaller flow amplitude,  $u_{\max} = 0.5$  are shown in Fig. 8. The averaging time was chosen to be  $\Delta t_{av} = 10$ . The case of Fig. 8a corresponds to a frequency of  $f = 0.01$  and it lies approximately at the threshold given by Eq. (22). The instantaneous velocity at the P→C cell indicates that the noise amplitude is nearly equal to the flow amplitude; as a consequence, the corresponding time-averaged velocity (shown in Fig. 8b) wanders around the analytical curve, clearly showing the traces of instantaneous fluctuations. At smaller frequencies the momentum spreads over the whole domain and the maximum velocity attained in the neighbourhood of the overlapping region is larger (recall that the Reynolds number depends on  $f^{-1/2}$ ). This explains why the simulation with  $f = 0.002$  in Fig. 8c is in better agreement with the analytical trend than that for  $f = 0.01$ . Finally, in Fig. 8c we present a case with  $u_{\max} = 0.5$  but at a larger temperature  $T = 4$ . The flow amplitude is then below the threshold given by Eq. (22) and forces arising from thermal fluctuations are larger than those arising from the mean flow.

## VII. CONCLUDING REMARKS

We have presented a hybrid finite volume formulation for the P→C coupling in our atomistic-continuum scheme based on the exchange of fluxes between both domains. The scheme has been used to perform hybrid simulations of the oscillatory shear flow driven by the harmonic motion of one of the walls of a nano channel. The particle domain (P) comprises one of the walls and a part of the adjacent fluid layer, while the remaining fluid within the slot is described by continuum fluid dynamics (CFD). The results show that the flux-coupling scheme is able to solve unsteady flows up to high characteristic frequencies corresponding to a Stokes number of  $St \equiv 2\pi f L_x^2 / \nu \leq O(100)$ .

A central part of this study has been focused on the limitations of the scheme due to the effect of the fluctuations arising from the particle domain. We found that in flows with low shear rates  $\gamma \leq O(10^{-2})$  fluctuations of velocity

and momentum flux may affect the continuity at the overlapping region. For  $\gamma \leq O(10^2)$  these fluctuations induce differences of the P and C velocities which are of the same size as the maximum flow velocity. This affects the flux-scheme because the momentum flux injected into the P region is measured from the local velocity gradient in the C domain. We were able to largely avoid this problem by implementing a finite volume scheme that uses a hybrid definition of the velocity gradient, constructed from a linear combination of the C-velocity and the averaged molecular velocity at the flux boundary condition for the C domain. The algorithm derived for time integration of the C velocity has an extra term that produces a seamless velocity profile by gently driving the C-velocity towards the averaged P-velocity. The strength of the coupling term is proportional to a coupling parameter  $\alpha \in (0, 1]$  and the scheme is not very sensitive to the value of  $\alpha$ , provided that  $\alpha > 0$  (we used  $\alpha \sim [0.1 - 0.5]$ ). It is important to mention that the *velocity coupling* term only acts on the C domain and has no direct effect on the particle dynamics. Such a procedure avoids the use of Maxwell demons within the overlapping region, which appear in schemes that rely on variable-coupling [26, 27]. Another attractive feature of the P→C coupling presented here is that it guarantees the velocity continuity while still preserving the balance of fluxes in the coarse-grained dynamics. Indeed, the use of hybrid gradients may be extended to any desired variable. For instance, in the case of diffusion of mass density, Flekkøy *et al.* [8] used a purely hybrid gradient (i.e., with  $\alpha = 1$  in the present notation) to couple random walkers with a finite difference description of Fickian diffusion.

If the signal-to-noise ratio  $E$  of the momentum flux is smaller than one the flow cannot be described using a deterministic scheme for the continuum flow. We have analysed this flow field resolution limit by calculating  $E$  using a route based on the Green-Kubo formalism. Resolution conditions are written in terms of the shear rate in Eq. (21) and in terms of the oscillatory-wall velocity in Eq. (22). Simulations performed near and below the derived resolution limit were shown to be consistent with the theoretical considerations. If the flow amplitude is smaller than the threshold given by Eqs. (21) or (22) the effect of fluctuations should also be taken into account by describing the C domain through a mesoscopic fluid model that solves the stochastic Navier-Stokes equations [28, 29]. In the case of Fickian diffusion, Alexander and coworkers used a hybrid particle-continuum algorithm to study the fluctuating hydrodynamic limit [30]. They considered a hybrid coupling scheme with both deterministic and stochastic continuum solvers and found that, if the correct stochastic representation is used within C, the mean and variance of the density are correctly coupled within the overlapping region. The authors showed that a deterministic hydrodynamic solver guarantees the coupling of the mean density fields, although in this case the variance falls exponentially in the direction of the continuum domain. We observed similar results in our simulations. The generalisation of our hybrid scheme to largely fluctuating flows is feasible and the implementation of a stochastic continuum solver would not substantially alter the scheme presented here.

### Acknowledgments

This research is supported by the European Commission through a Marie Curie Fellowship to RD-B (HPMF-CT-2001-01210) and by the EPSRC RealityGrid project GR/R 67699. R.D-B also acknowledges support from project BFM2001-0290.

- 
- [1] F.F.Abraham, J. Broughton, N. Berstein, and E. Kaxiras, *Europhys Lett.* **44**, 783 (1998).
  - [2] A. Garcia, J. Bell, W. Y. Crutchfield, and B. Alder, *J. Comp. Phys.* **154**, 134 (1999).
  - [3] R. Delgado-Buscalioni and P. V. Coveney, *Phys. Rev. E* **67**, 046704 (2003).
  - [4] E. G. Flekkøy, G. Wagner, and J. Feder, *Europhys. Lett.* **52**, 271 (2000).
  - [5] G. Wagner, E. Flekkoy, and T. Jossang, *Computer Physics Communications* **147**, 670 (2002).
  - [6] C. Wijmans and B. Smit, *Macromol.* **35**, 7138 (2002).
  - [7] A.D.Stroock, S. Dertinger, A. Ajdar, and I. Mezić, *Science* **295**, 647 (2002).
  - [8] E. G. Flekkøy, J. Feder, and G. Wagner, *Phys. Rev. E* **64**, 066302 (2001).
  - [9] S. Hess, M. Kroger, and H. Voigt, *Physica A* **250**, 58 (1998).
  - [10] M. Allen and D. Tildesley, *Computer Simulations of Liquids* (Oxford University Press, 1987).
  - [11] D. Frenkel and B. Smith, *Understanding molecular simulations* (Academic Press, London, 1996).
  - [12] P. A. Thompson and M. O. Robbins, *Phys. Rev. A* **41**, 6830 (1990).
  - [13] C. Trozzi and G. Ciccotti, *Phys. Rev. A* **29**, 916 (1984).
  - [14] D. M. Heyes, *Chem. Phys. Lett.* **153**, 319 (1988).
  - [15] S. V. Patankar, *Numerical Heat Transfer and Fluid Flow* (Hemisphere, New York, 1980).
  - [16] M. J. Vogel, A. H. Hirs, and J. M. Lopez, *J. Fluid Mech.* **478**, 197 (2003).
  - [17] D. J. Evans and G. P. Morris, *Statistical Mechanics of Nonequilibrium Liquids* (Academic Press, London, 1990).
  - [18] K. Johnson, J. A. Zollweg, and K. E. Gubbins, *Mol. Phys.* **78**, 591 (1993).

- [19] S. Barsky, R. Delgado-Buscalioni, and P. V. Coveney, *Comparison of molecular dynamics with hybrid continuum-molecular dynamics computational fluid dynamics for a single tethered polymer in a solvent* (2004), arxiv.org/cond-mat/0401392.
- [20] R. Delgado-Buscalioni and P. V. Coveney, *J. Chem. Phys.* **119**, 978 (2003).
- [21] R. Zwanzig and R. Mountain, *J. Chem. Phys.* **43**, 4464 (1965).
- [22] S. Hess, M. Kroger, and W. G. Hoover, *Physica A* **239**, 449 (1997).
- [23] L. D. Landau and E. M. Lifshitz, *Fluid Mechanics* (Pergamon Press, 1959).
- [24] H. Schliting, *Grenzschicht-Theorie* (Braun, Karlsruhe, 1958).
- [25] H. Carslaw and J. Jaeger, *Conduction of Heat in Solids, 2nd ed.* (Clarendon Press, Oxford, 1959).
- [26] D. L. J. Li and S. Yip, *Phys. Rev. E* **57**, 7259 (1998).
- [27] S. T. O'Connell and P. A. Thompson, *Int. J. Mod. Phys. C* **52**, R5792 (1995).
- [28] M. Serrano and P. Español, *Phys. Rev. E* **64**, 046115 (2001).
- [29] E. Flekkøy, P. Coveney, and G. D. Fabritiis, *Phys. Rev. E* **62**, 2140 (2000).
- [30] F. J. Alexander, A. L. Garcia, and D. M. Tartakovsky, *J. Comp. Phys* **182**, 47 (2002).
- [31] Note that for a regular grid the finite volume discretization of Eq. (7) coincides with the explicit finite difference version.
- [32] As shown in Ref. [20], to insert an LJ atom at a location where the potential energy equals the mean specific potential energy of the system the USHER algorithm needs around 30 iterations if the mean density is  $\rho_c \simeq 0.8$ , and 15 iterations if  $\rho_c \simeq 0.7$  (each iteration corresponding to the evaluation of a single-particle force).

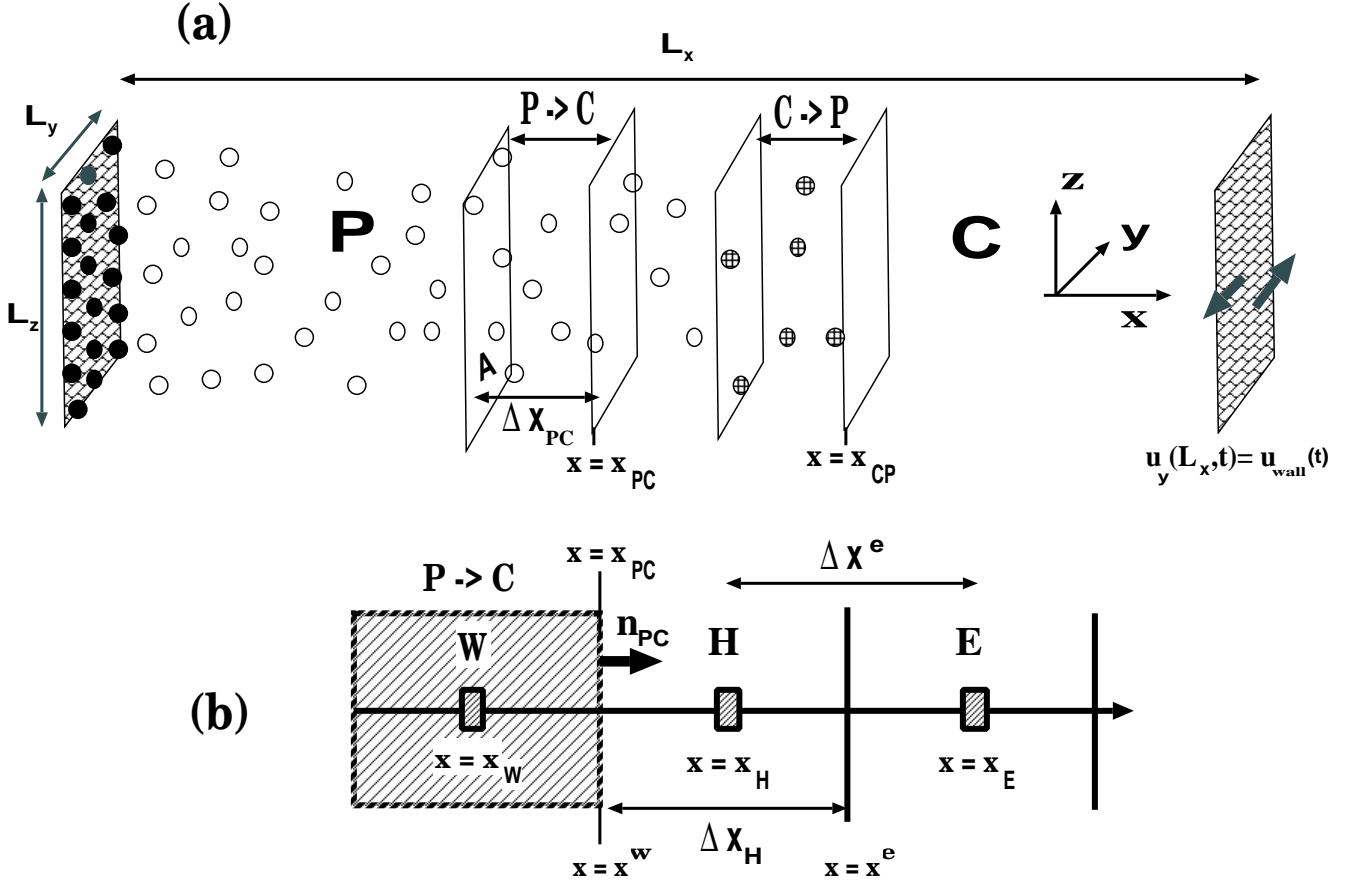


FIG. 1: The domain decomposition of the hybrid scheme. (a) displays the set-up used in the present work (periodic in  $y$  and  $z$  direction) indicating the particle domain (P), the continuum domain (C) and the handshaking domain comprised of the C→P and P→C cells, whose surface area is  $A$ . The P domain is contained in  $x \leq x_{CP}$  and includes the wall around  $x \sim 0$  formed by two layers of LJ atoms in a hexagonal lattice (black circles). The C domain is  $x_{PC} \leq x \leq L_x$  and includes a boundary condition at  $x = L_x$ , which imposes  $u_y(L_x, t) = u_{wall}(t)$  (moving wall). Open circles represent particles whose dynamics are uniquely determined by their corresponding intermolecular forces. Particles entering the C→P cell (hatched circles) feel extra forces coming from the continuum domain. (b) shows three consecutive cells of the finite volume discretization of the C domain:  $H$ ,  $W = H - 1$  and  $E = H + 1$ . The index of the cell centres runs from  $H = 1$  to  $H = M$ . For the first cell  $H = 1$ , whereas the west cell  $W (= 0)$  is outside the C domain and within the P→C buffer, as indicated in (b) (see Sec. III). The centre-to-centre distance is  $\Delta x^e = x_E - x_H$  and the face-to-face distance is  $\Delta x_H = x^e - x^w$ .

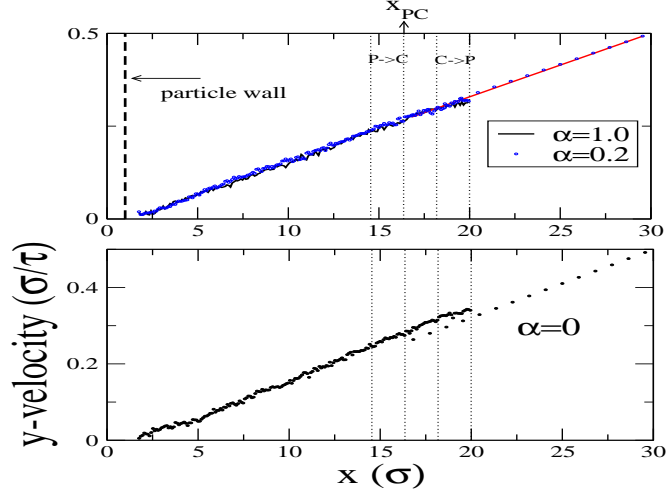


FIG. 2: The  $y$ -velocity versus the  $x$  coordinate for tests done in a Couette flow with wall velocity  $u_{\max} = 0.5$ . The particle region comprises  $x \leq 20$  and the continuum domain is  $x \in [16.36, 30]$ . The mean density is  $\rho = 0.8$  and the temperature is  $T = 1.0$ . Vertical lines indicate the average  $x$  position of particle wall ( $x = 1$ ), the P→C interface  $x_{PC} = 16.31$  and the extent of the P→C and C→P cells,  $\Delta x_{PC} = 1.81\sigma$ . The upper figure shows the  $y$ -velocities averaged over  $\sim 800\tau$  obtained for  $\alpha = 1$  and  $\alpha = 0.2$ . The lower figure shows the  $y$ -velocities obtained using  $\alpha = 0$ , averaged over  $\sim 700\tau$ .

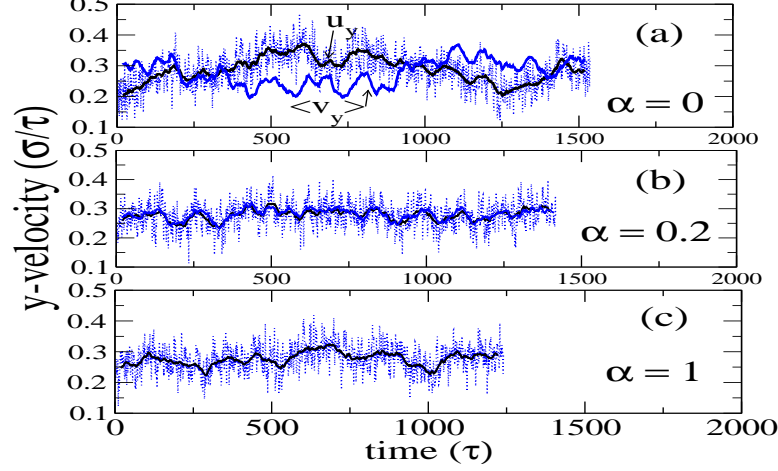


FIG. 3: The effect of the  $\alpha$  parameter in Eq. (11) on the continuity of the  $y$ -velocity at  $x_1 = x_{PC} + \Delta x/2$  ( $x_{PC} = 16.31$  and  $\Delta x = 0.9$ ) for the same Couette flow tests shown in Fig. 2. From top to bottom the figures correspond to  $\alpha = 0$ ,  $\alpha = 0.2$  and  $\alpha = 1$ . The continuum velocity at  $x = x_1$  is labelled by  $u_y$  and the mean particle velocity within the region  $|x - x_1| \leq 0.9$  is denoted as  $\langle v_y \rangle$ . Dotted lines correspond to velocities averaged over a short time interval  $\Delta t_{av} = 1\tau$ , and solid lines are the same velocities averaged over  $20\tau$ . The velocities  $u_y$  and  $\langle v_y \rangle$  are indicated in (a), while in (b) and (c) their values are almost identical. Note that the size of the velocity discontinuity observed for  $\alpha = 0$  is similar to the amplitude of the velocity fluctuations (dotted lines).

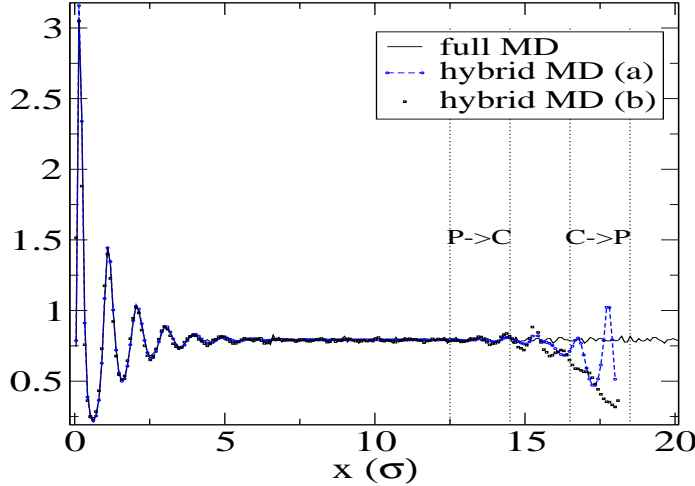


FIG. 4: The particle density versus the direction normal to the atomistic wall at  $x \leq 0$  for a WCA-LJ fluid of density  $\rho_c = 0.8$  and temperature  $T = 1.0$ . The density profile obtained with the hybrid scheme is compared with the outcome of a full MD simulation with a second atomistic wall at  $x = 50\sigma$ . (a) corresponds to  $\rho_O = 0.7$  in Eq. (14) and (b) to  $\rho_O = 0.5$ . The width of the C $\rightarrow$ P cell is  $\Delta x_{CP} \simeq 2.3\sigma$ . The locations of the P $\rightarrow$ C and C $\rightarrow$ P cells are also shown (see Sec. IV B for further details).

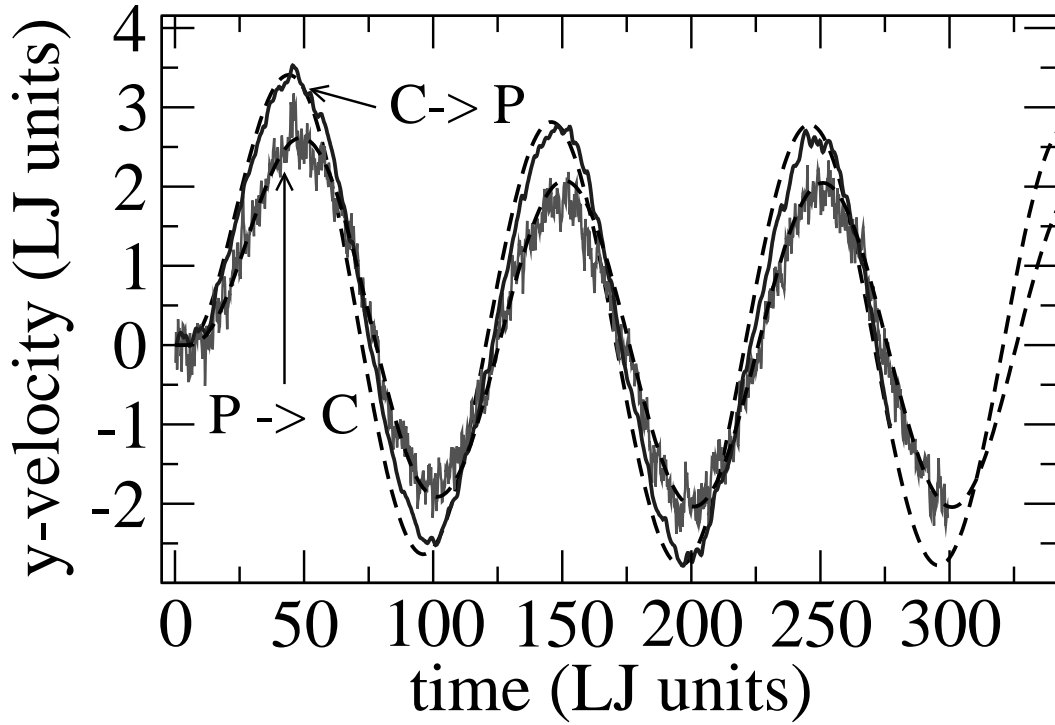


FIG. 5: The velocity within the overlapping region for an oscillatory flow with wall velocity  $u_{wall}(t) = u_{max} \sin(2\pi ft)$ , of amplitude  $u_{max} = 10$  and frequency  $f = 0.01$ . The particle domain comprises  $x = [0, 21]$  and the continuum  $x \in [17, 30]$ ; the extent of the periodic directions is  $L_y = L_z = 9$ . The nanochannel is filled with a LJ fluid at  $\rho = 0.8$  and  $T = 1.0$ . We plot the instantaneous particle velocity at the P→C cell (noisy signal) and the time-averaged velocity over  $\Delta t_{av} = 1$  at the C→P cell. Dashed lines correspond to the analytical solution of the flow.

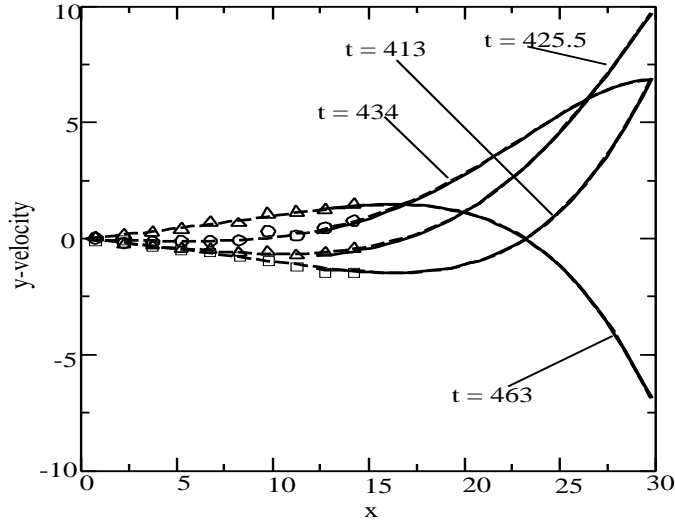


FIG. 6: Snapshots of the  $y$ -velocity versus the  $x$  coordinate at several instants in time for the same flow as in Fig. 5. The particle domain comprises  $x \in [0, 15]$  and the continuum region  $x \in [12, 30]$ . The mean velocities within the P region are calculated within slices of width 1.6 and averaged over  $\Delta t_{av} = 1$ ; these velocities are plotted using different symbols for each time instant. We used  $\alpha = 0.5$  in Eq. (11). The solid lines correspond to the solution within the continuum region, solved via a finite volume scheme, and the dashed lines are the analytical solutions. All quantities are given in reduced LJ units.



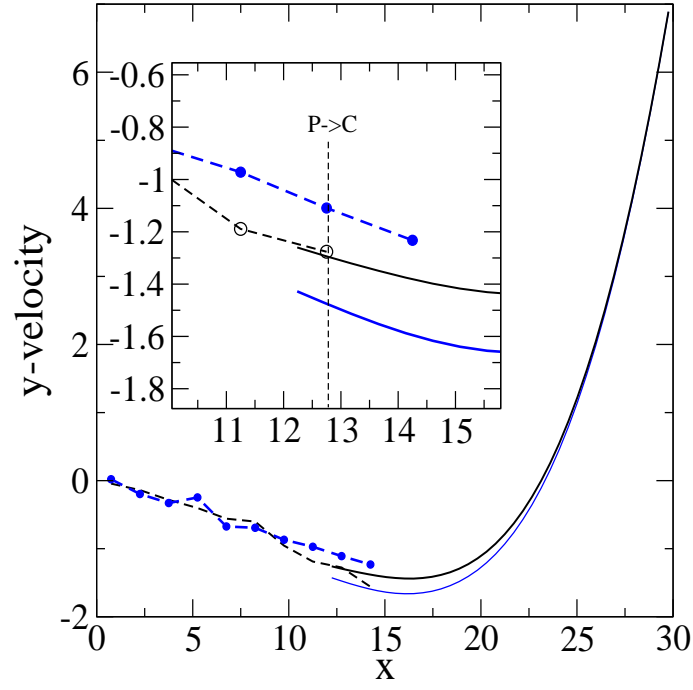


FIG. 7: Comparison of the velocity profiles obtained with  $\alpha = 0.5$  and  $\alpha = 0$  in Eq. (11). The parameters are those of Figs. 5 and 6. Results were obtained with  $\Delta t_{av} = 1$ . The velocity discontinuity observed in the  $\alpha = 0$  calculation (about 0.4) is of the same order of magnitude as the variance of the mean velocity within the P→C cell. All quantities are given in reduced LJ units.

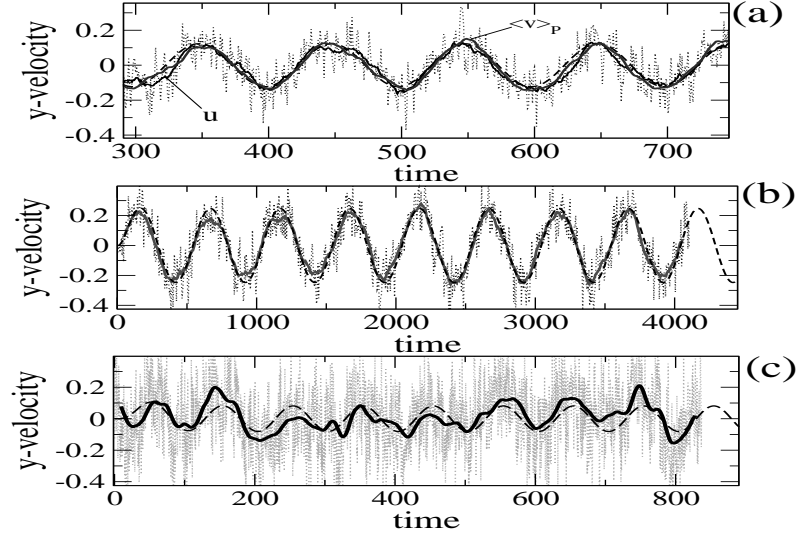


FIG. 8: The mean particle velocity in oscillatory shear flows with  $u_{\max} = 0.5$  and  $\rho = 0.8$ . The molecular dynamics domain comprises  $x \in [0, 20]$  and the continuum  $x \in [16.36, 30]$ , the velocity is evaluated within the P→C cell (around  $x = 17.27$ ). (a) corresponds to  $T = 1$  and  $f = 0.01$ ; (b) to  $T = 1$  and  $f = 0.002$  and (c) to  $T = 4$  and  $f = 0.01$ . Solid lines correspond to the time-averaged mean particle velocity (in time intervals  $\Delta t_{av} = 10$ ), dotted lines to the instantaneous mean velocity and dashed lines to the analytical solution of the flow. In (a) we show the time-averaged mean particle velocity  $\langle v \rangle_P$  along with the continuum velocity  $u$  at the same location.